Additive Manufacturing Benchmark 2022 Subcontinuum Mesoscale Tensile Challenge (CHAL-AMB2022-04-MeTT) and Summary of Predictions*

Orion L. Kafka (0000-0003-2333-8154)[1*†], Jake Benzing (0000-0002-7266-870X)[1*†], Newell Moser (0000-0002-3346-6427)[1], Li-Anne Liew (0000-0003-0202-026X)[1], Jordan Weaver (0000-0003-4857-5164)[2], Nikolas Hrabe (0000-0001-7585-0980)[1*]

[1]Material Measurement Laboratory, National Institute of Standards and Technology, 325 Broadway St, Boulder, 80305, CO, USA.
[2]Engineering Laboratory, National Institute of Standards and Technology, 100 Bureau Drive, Gaithersburg, 20899, MD, USA.

*Corresponding author(s). E-mail(s): orion.kafka@nist.gov; jake.benzing@nist.gov; nik.hrabe@nist.gov;
Contributing authors: newell.moser@nist.gov; li-anne.liew@nist.gov; jordan.weaver@nist.gov;
†These authors contributed equally to this work.

Abstract

This additive manufacturing benchmarking challenge asked the modelling community to predict the stress-strain behavior and fracture location and pathway of an individual meso-scale (gauge dimensions of approximately 200 µm thickness, 200 µm width, 1 mm length) tension specimen that was excised from a wafer of nickel allow IN625 manufactured by laser powder bed fusion (L-PBF). The data used for the challenge questions and answers are provided in a public dataset (https://data.nist.gov/od/id/mds2-2587). Testing models against the data is still possible, although a good-faith blinded prediction should be attempted before reading this article, as the results are contained herein. The uniaxial tension test

was pin loaded, conducted at quasi-static strain rates under displacement control, and strain was measured via non-contact methods (digital image correlation). The predictions are challenging since the number of grains contained in the thickness of the specimen are sub-continuum. In addition, pores can be heterogeneously distributed by the L-PBF process, as opposed to intentionally seeded defects. The challenge provided information on chemical composition, grain and sub-grain structure (surface-based measurements via electron backscatter diffraction and scanning electron microscopy) and pore structure (volume-based measurements via X-Ray computed tomography) along the entire gauge length for the tension specimen. During the challenge, prediction responses were collected from six different groups. Prediction accuracy compared to the measurements varied, with elastic modulus and strain at ultimate tensile strength consistently over-predicted, while most other values were a mix of over- and under-predicted. Overall, no one model performed best at all predictions. Failure-related properties proved quite challenging to predict, likely in part due to the data provided as well as the inherent difficulty in predicting fracture. Future directions and areas of improvement are discussed in the context of improving model maturity and measurement uncertainty.

Keywords: Additive Manufacturing, Benchmark Challenge, Mechanical Properties, Tensile Testing, Subcontinuum

1 Introduction and Challenge Formulation

Enabling the predictable and repeatable performance of additively manufactured components is part of the Additive Manufacturing (AM) Research and Development mission at the National Institute of Standards and Technology (NIST). Establishing processing-structure-property relationships through advanced measurement science is a well-accepted practice to fulfill this mission, but a full design of experiments is usually limited by time and other valuable resources. Modelling efforts and simulations provide a solution to this by rapidly narrowing selection windows based on predicted performance. Moreover, the rapid iteration of product designs used in modern engineering practice requires reliable and precise predictions. In order to prove model capabilities, somewhat blind predictions are necessary to assess the strengths and weaknesses of a given approach. Hence, the need for challenges exists.

Two notable previous challenges have been conducted, which target somewhat similar application spaces. The third Sandia fracture challenge [1] provided uniaxial tensile properties, grain structure information, pore population information, and more (calibration data) for 316L stainless steel material manufactured by laser powder-bed fusion (L-PBF). The challenge asked for predictions of the ductile failure path in a specimen geometry that included internal channels of varying angles and shapes that could not have been conventionally machined. This testing was performed by Sandia National Laboratories, and the answers were not released until all predictions were submitted. The results showed that most submissions were able to predict the nominal crack path and initiation location correctly, but the accuracy had improved since

the second Sandia fracture challenge, indicating increased maturity for many types of models. One major limitation of the challenge was its reliance upon predefined macroscopic defects that inherently reduce the generally stochastic nature of failure. In the following year, the Air Force Research Laboratory (AFRL) launched a four-part challenge series bridging either processing-to-structure or structure-to-properties relationships on macro- and micro-scale length scales [2]. With respect to the current work, specifically micro-scale property prediction from microstructure, AFRL Challenge 3 asked for predictions of aggregate macro-scale stress-strain behavior (microstructure provided) whereas Challenge 4 asked for predictions of elastic strain in a particular grain (explicit 3D microstructure provided) for nickel alloy 625 (IN625) material produced by laser powder bed fusion, but all requested values were prior to the onset of localization and did not involve failure. In the report on lessons learned, the modeling community voiced a need for clear definitions and descriptions of data. However, the consensus was that the longer term, more impactful outcome of the challenge series is the curated, publicly available data that is available in perpetuity. Based on potential gaps observed in the results and lessons learned from previous challenges, the AM-Bench 2022 Subcontinuum Mesoscale Tensile Challenge (AMB2022-04-MeTT) was formulated.

AMB2022-04 is a direct extension to the measurement data provided by the first Additive Manufacturing Benchmark Challenge (AMB2018-01) [3]. For AMB2018-01, data were provided for L-PBF builds of IN625, including powder characterization, detailed information about the build process, in situ measurements during the build, ex situ measurements of the residual stresses, part distortion following partial cutting off the build plate, location-specific microstructure characterization, and microstructure evolution during a post build heat treatment. Here, these data are extended to include mechanical property data for the as-built material. An additional build plate of parts designed for mechanical testing was fabricated using the same build machine as AMB2018-01, the same alloy (different lot number), and a different bulk material scan pattern. These parts were used for meso-scale mechanical testing, with additional characterization provided by both X-ray Computed Tomography (XRCT) and scanning electron microscopy (SEM) along the entire gauge volume and length. The mechanical test specimen reported here was measured in the as-built state, with no residual stress/anneal. Predictions of elastic modulus, stress at specific values of true strain (i.e., 0.2 % true strain offset yield stress, stress at 0.05 mm/mm total true strain, and ultimate tensile strength (UTS)), true strain at UTS, and fracture location (i.e., distance from reference point to each side of the reduced cross-section "necked" region and average fracture surface) and reduction in width were requested. In total, six sets of predictions were submitted and compared against experimentally determined values, while taking measurement uncertainty into consideration when scoring the models. Scoring used one standard uncertainty from the experimental measurements as the base metric, i.e., models within the uncertainty were considered to have correctly predicted the outcome.

The remaining four sections of this challenge description and results summary are organized into (2) Materials and Methods, (3) Experimental Results, (4) Discussion,

and (5) Conclusions. The materials and methods section describes information necessary to replicate the build information, part design, tensile testing, as well as methods used to characterize grain structure, pore structure, specimen geometry, and fracture behavior via SEM, and XRCT. The results section is broken down into distinct sections of results that were provided to the modellers when challenges were announced, and the results provided after the submission deadline had closed, meaning the extra results used to score the submissions. In the discussion section, the models and results from each submission are compared to the value acquired with the experimental measurements, and lessons learned are summarized from a post-challenge workshop that took place a few months after the AM Bench 2022 Conference. Future directions are also included. Conclusions on efficacy or not of models are made for this blind prediction and major areas of improvement are identified.

2 Materials and Methods

2.1 Build information and part design

The build plate reserved from AMB2018-01 and the new build plate of specimens for mechanical testing were both built on the same EOS M270[1]. The EOS M270 is referred to using the designation CBM, for commercial build machine. To the greatest extent possible, the build parameters and conditions were kept identical between the AMB2018 and AMB2022 builds, but new powder lots were required because there was insufficient IN625 powder remaining from AM Bench 2018. The new build plate was designated AMB2022-625-CBM-B1.

The new AMB2022-04 build was conducted using IN625 powder with chemical composition provided in Table 1. Values in the table were taken from vendor-supplied data sheets, which utilized ASTM E1479 [4] (inductively-coupled plasma atomic emission spectrometers) for all elements except for using ASTM E1019 [5] (combustion) for C/S and ASTM E1019 (fusion) for O/N. The powders were kept sealed in the original shipment containers until use. Virgin powder was used. Chemical composition for as-built solid material was measured after the build and is also provided in Table 1. Alloy IN625 is often used as an intermediate-to-high temperature material, and are effective at resisting creep and rupture in corrosive and oxidizing environments, which makes it industrially appealing. Generally, parts are made by forging, which results in a homogeneous, solid solution strengthened microstructure. Forged and annealed IN625 has a specified 827 MPa tensile strength with 30% elongation [6]. When made with L-PBF, the microstructure tends to be columnar. The microstructure and composition are relatively simple, for an AM alloy, but the alloy nevertheless has fair industrial applicability, which is why this alloy was selected for the initial AM Bench work. The current paper follows along that legacy. Further details regarding the alloy have been reported in previous AM Bench work (see [3] and the rest of the "Additive Manufacturing Benchmarks 2018" topical collection).

[1] Certain commercial equipment, instruments, or materials are identified in this paper in order to specify the experimental procedure adequately. Such identification is not intended to imply recommendation or endorsement by NIST, nor is it intended to imply that the materials or equipment identified are necessarily the best available for the purpose.

Table 1 Elemental composition of powder feedstock and solid material. All composition measurements are in mass percent. The standard composition is defined by ASTM B564-22, UNS N06625 [6] (maximum unless range or minimum is noted).

Element	Standard	Powder	Solid
Ni	58.0 Min	Balance	Balance
Cr	20.0-23.0	21.54	20.4
Fe	5	0.78	1.00
Mo	8-10	9.19	8.60
Nb	3.15-4.15	4.13	3.83
Co	—	0.18	n/a
Ti	0.4	0.38	0.31
Al	0.4	0.32	0.27
Si	0.5	0.14	0.11
Mn	0.5	0.05	0.06
P	0.015	<0.01	<0.001
Ta	—	0.02	n/a
C	0.10	0.02	0.02
S	0.015	<0.005	0.009
O	n/a	0.01	n/a
N	n/a	0.01	0.21

Table 2 CBM nominal build conditions. [1]Estimated. [2]Measured at build chamber ceiling

Infill laser power (W)	195
Infill scan speed (mm/s)	800
Hatch spacing (µm)	100
Nominal layer thickness (µm)	20
Infill laser diameter, at recoating plane[1] (µm D4σ)	100
Infill laser diameter[1] (µm FWHM)	59
Inert gas	Nitrogen
Oxygen level (% $\pm$ 1 Std Dev)[2]	0.58 ± 0.07

The nickel alloy IN625 parts were built on a full size (252 mm $\times$ 252 mm) 1045 steel alloy build plate. N_2 cover gas with low velocity was used. Figure 1a shows a diagram of the AMB2022-625-CBM-B1 build plate, along with specimen extraction. This plate included eight macroscale tensile specimens (T1-T8), three parts designed to provide material for mesoscale tensile specimens for this challenge (TH1-TH3), and several additional parts for general purpose use. The part labels on Figure 1a were appended to the build plate ID to provide unique identifiers for the individual parts. For example, AMB2022-625-CBM-B1-TH1 refers to the mesoscale tensile block labeled TH1 in Figure 1a.

The portions of blocks TH1-TH3 used for mesoscale tensile testing and all microstructure characterization used an X-only scan strategy with no scan rotation between layers. A 100 mm stripe width was used, and the parts were located such that characterized material did not contain stripe boundaries. Detailed build parameters are summarized in Table 2

Although in practice heat treatments (annealing or solution annealing) are commonly applied to this alloy ([6]) to enable high service temperature operation, no heat treatment was applied to this material. A wafer (nominal dimensions 10 mm × 24.34 mm × 0.45 mm) was cut from section F of block TH1 (Figure 1b) using wire electric discharge machining (EDM). EDM was then used to cut a meso-tensile specimen from that wafer (Figure 1c-d). The design of the meso-tensile specimen was from previous work [7].

The 0.45 mm thick meso-scale tensile specimen was thinned to an approximate thickness of 0.24 mm (see exact measurements in Table 3 and Figure 3) using standard machine polishing procedures: SiC grinding paper, 1 µm diamond particle suspension and 50 nm colloidal silica. This sample preparation method was completed so that one side of the entire specimen and thus gauge length could be analyzed using the SEM and was based on methods used in previous work [8]. A fiducial mark was applied to one grip section of the specimen to enable repeatable microstructural measurements before and after tensile deformation (Figure 5a).

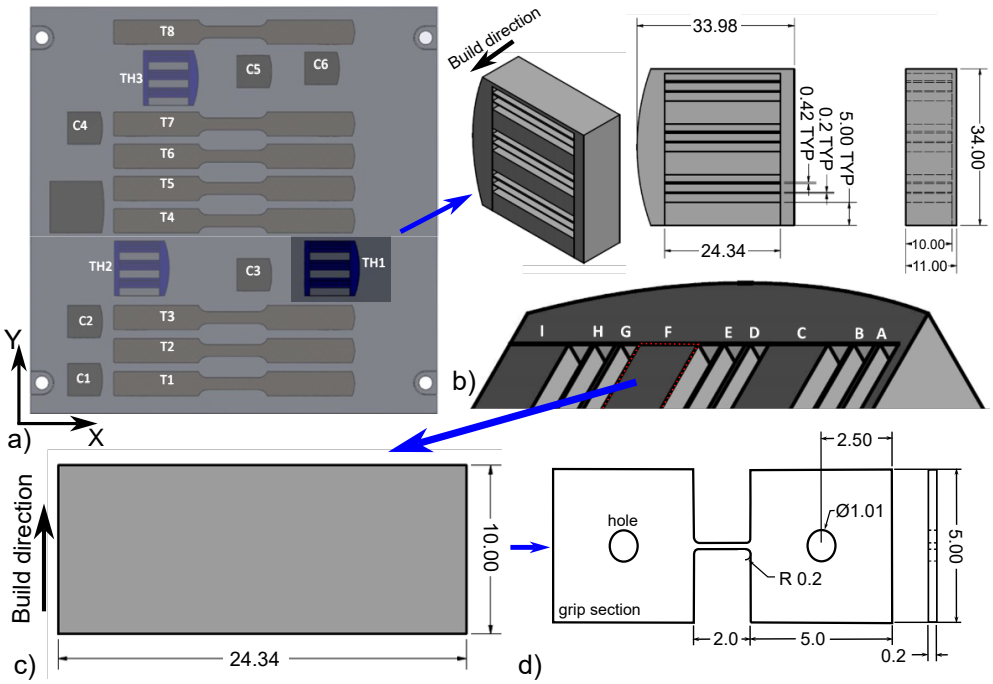

Fig. 1 Schematic of (a) build layout, (b) part on the layout, (c) material extracted from that part, and (d) the final specimen geometry that was tested. Units in mm.

2.2 Mesoscale tensile testing

The tensile tests of the mesoscale specimens were carried out using a commercial screw-driven miniature universal testing stage from Fullam Inc., which was originally designed for in-situ SEM testing. [2] The specimens were held in custom clevises with 1 mm diameter pins. No through-thickness forces were applied to the specimen. Based on previous experience, deformation outside the gauge section of the meso-tensile specimen was be assumed to be negligible. The tensile tests were performed ex-situ under an optical microscope with a 2X objective lens, at a strain rate of $0.001\,\mathrm{s}^{-1}$, and at room temperature. The average strain rate of $0.001\,\mathrm{s}^{-1}$ was determined from the measured specimen displacements from the images during the test, which is about 2.2 µm/s The crosshead speed was Papproximatesly 300 µm/s. The load cell (250 N capacity, from Omega Engineering) was last calibrated in November 2019 and has a force uncertainty of 0.5 N, and was rechecked in February 2022. Force uncertainty and cross-sectional area uncertainty are combined to compute stress uncertainty. Photographs of the test setup can be found in [7]. Images were captured using a Jenoptik camera with an image resolution of 3072 pixels × 2300 pixels. Strain was measured using digital image correlation (DIC) to conduct 2-point extensometry. An example image used for DIC is shown in Figure 2. The images were analyzed offline, using DIC, to obtain displacements in pixels, from which the engineering strains are calculated. To avoid potential damage to the small and fragile specimen, the as-produced (wire EDM) surface was used as the speckle pattern for DIC; no additional speckling was conducted. A custom DIC program was used, which has been benchmarked against known deformations (i.e., pre-deformed image pairs) and a commercial DIC program (VIC2D) [9]. One square DIC subset with an edge length of 64 pixels was placed at each end of the uniform section of the gauge, about 840 µm from the center of the gauge. Engineering stress was computed from load cell force measurement and mean area as measured by XRCT, see Section 2.4. Stress uncertainty was computed from load cell calibration uncertainty and and area measurement uncertianty. True stress and strain were computed from the engineering values, according to the equations: $\sigma_{true} = (\sigma_{eng.})(1+\varepsilon_{eng.})$, and $\varepsilon_{true} = \ln(1+\varepsilon_{eng.})$ (i.e., logarithmic or Hencky strain, under the assumption of volume conservation). For simplicity, in the 1D tensile loading case employed here, we will use scalars true stress and true strain to express the deformation relationship.

For the DIC measurements, strain uncertainty is computed by assuming a 0.2 pixel absolute displacement uncertainty in the DIC measurement, and dividing this by the current displacement to compute relative displacement uncertainty. The 0.2 pixel displacement uncertainty is derived from earlier tests of a similar but not necessarily identical setup. Stationary image tests with the DIC give spurious strains of order 1×10^{-5} mm/mm. Out plane motion of 250 µm results in a spurious strain of about ±0.001 mm/mm with our setup. However, defocusing of the specimen occurs at about 150 µm, and the images we captured during testing have no perceptible loss of focus under a 10X objective indicating a out of plane drive of significantly less than 150 µm. Thus, out of plane motion did not result in spurious strains greater than our 0.2 pixel

[2] This commercial test stage was manufactured in the 1990's to early 2000's and documentation on its specifications are scarce as the vendor no longer exists.

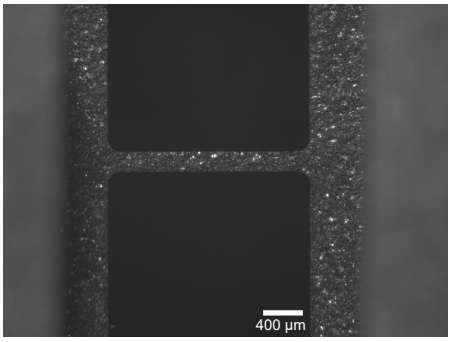

Fig. 2 Example image used for DIC-based strain measurement; the inherent pattern of the wire EDM surface is used as the speckle pattern.

uncertainty floor. Relative gauge length uncertainty was computed from absolute length uncertainty, taken as the DIC subset size (64 pixels divided by the absolute length, in this case 1138 pixels (the length of the gauge section in the camera field of view). Engineering strain uncertainty is then the quadrature addition of the relative uncertainties in gauge length and displacement. These were then propagated into true values for each value of strain. Further discussion of the measurement uncertainties related to this test system are discussed in Ref. [10].

2.3 SEM metallography

Electron backscatter diffraction (EBSD) measurements were performed on two orthogonal planes using a field emission scanning electron microscope operated with the following parameters: 20 kV accelerating voltage, 120 µm aperture, 19 mm working distance, 500X magnification and dynamic focus. The multi-tile EBSD acquisition parameters were: 4x4 binning, 100 frames per second, multiple tiles with 5 % overlap, 0.25 µm step size and the Nickel phase index.

Backscattered electron images were acquired with a field-emission SEM on two orthogonal planes (XZ and XY, where Z is the build direction) using the following parameters: 20 kV accelerating voltage, 60 µm aperture, and 8.5 mm working distance. During the EDM process, a re-cast layer is generated on surfaces that are not eventually polished, but experimental observation determined the thickness of this layer is less than 1 µm.

2.4 X-ray computed tomography

X-ray computed tomography (XRCT) was used to measure pores and changes in specimen dimensions in 3D throughout the gauge section. These two data were used to compute porosity and cross-sectional area as a function of height (i.e., gauge length).

Specifically, the sub-continuum specimen was mounted vertically in a sample holder, such that the deformation direction (X) is perpendicular to the resultant image slices. XRCT scans were conducted with voxel-edge-length of approximately 1.0 µm. The scans consisted of collecting 2401 projection images while rotating the specimen

through 360°. Vertical Stitching mode with multiple scans was used to increase the vertical field of view to cover the full specimen.

The resulting projection images were reconstructed and stitched together using machine-specific proprietary software (Zeiss Reconstructor Scout-and-Scan ver. 14.0.14829). Once reconstructed and stitched, the image slices were exported to a stack of grayscale, 16-bit, 2D tagged image format file (TIFF) images, where each 2D image (or slice) represents one voxel-height of the specimen. In total, 2202 slices were required to represent the full specimen. These slices were then analyzed using a custom, NIST-developed Python toolkit [11].

The cross-sectional area and total porosity were computed after the reconstructed grayscale images were binarized (or segmented). The binarization procedure was:

1. Grayscale intensities above or equal to 33000 were made white (i.e., grayscale intensity of 65535. Conversely, all grayscale intensities below 33000 were made black (i.e., an intensity of 0).
2. Convert the data type to 8-bit. White pixels now correspond to a grayscale value of 255; black pixels still correspond to 0.

Example image slices before and after binarization are shown in Figure 3a, and a rendering of the resulting 3D image is shown in Figure 3b.

Additional analyses were performed to calculate the cross-sectional area and overall porosity based on these segmented images, where white pixels correspond to metal material and black pixels correspond to air/voids. Only image-slices along the gauge section, as well as a few corresponding to the initiation of the fillets, were considered for these additional analyses – specifically, image numbers 100 through 2070 were chosen. To calculate porosity, d_p, the following formula was used,

$$d_p = \frac{n_{void}}{(n_{metal} + n_{void})} \tag{1}$$

where n_{metal} is the total number of white pixels (that correspond to metal material), and n_{void} is to the total number of black pixels that correspond to fully enclosed voids. Fully enclosed is taken to mean black pixels that are surrounded in 3D by white pixels based on 1-connectivity. Porosity can range from zero to one, where zero implies a perfect build absent of any (detectable) voids. For this subcontinuum sample, the porosity along the gauge length was found to be: $d_p = 0.000052032$.

The cross-sectional area as a function of relative gauge length was also calculated using the aforementioned segmented images. For each segmented image-slice, the total number of white pixels (corresponding to metal material) was summed and then converted to µm^2 using the voxel-edge-length of approximately 1.0 µm/pixel. By doing this summation for each image-slice within the gauge region, the local cross-sectional area was calculated (Figure 3c). To be clear, the tensile axis of the subcontinuum sample is not guaranteed to be perfectly aligned to the cross-section illustrated in the reconstructed image-slices from XRCT due to small misalignments while mounting the sample in preparation for XRCT. As a consequence, the reconstructed image-slices are not perfectly aligned with the cross-sectional planes of the sample. However, based on the projection images, we have estimated this misalignment error to be less than

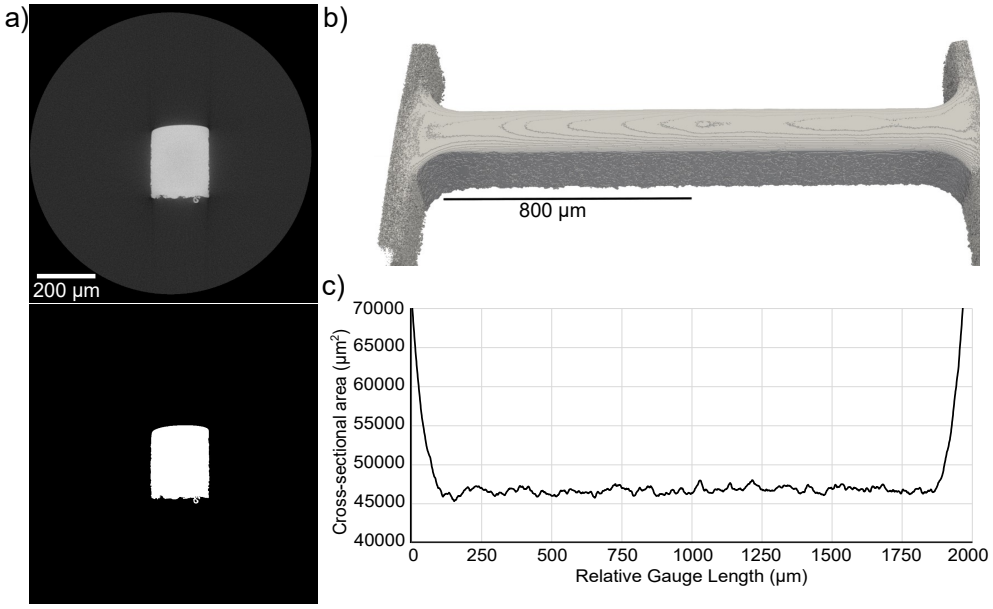

Fig. 3 a) grayscale and binarized (segmented) cross-sectional image slices, b) rendering from X-ray CT data of full gauge section, c) cross-sectional area computed from X-ray CT as a function of gauge length

1°. Additional details about the XRCT parameters and the post-processing steps can be found in the data repository [12].

2.5 Other material characterization

Material from AM Bench 2018 [13, 14] was deemed to be substantially similar to the new build, and thus the previous results were used in the current work. The material was built on the same machine with the same material (different powder lot) and different scan strategy (XY versus X-only).

2.5.1 Dislocation density (high energy X-ray diffraction)

The dislocation density in as-built IN625 was estimated using high-resolution synchrotron X-ray diffraction (XRD) data acquired at beamline 11-BM-B at the Advanced Photon Source (APS), Argonne National Laboratory [15]. The monochromatic X-ray energy was 30 keV (wavelength λ =0.041 455 4 nm). The X-ray flux density was approximately 5×10^{11} photons $s^{-1}mm^{-2}$. The beam size was 500 µm × 200 µm. The instrument was calibrated using NIST standard reference 660a (LaB6: lanthanum hexaboride). The samples were thinned to about 100 µm in thickness and the thin foil was cut into strips with an approximate dimension of 1 mm × 10 mm × 0.1 mm. The strips were loaded in Kapton capillaries and mounted on the standard sample holders of the beamline. During data collection, the samples spun rapidly in the beam (at about

3000 revolutions per minute). All measurements were conducted at room temperature (approx. 298 K). More details about the measurements can be found elsewhere [13].

For this analysis, the XRD data was acquired from sample 625-CBM-B1-P4-L4, as identified in [13] from AM Bench 2018. We performed peak profile analysis of seven reflections of IN625 (111, 200, 220, 311, 400, 331, and 420) using pseudo-Voigt functions. The centers are described as 2θhkl and the full-width at half maximum (FWHM) as whkl, where hkl represents the Miller indices. Because the instrument has a high q resolution $\Delta q/q \approx 10^{-4}$, instrumental broadening could be neglected the analysis. Scherrer's equation $D = \kappa\lambda/(\text{whkl} \times \cos(\theta\text{hkl}))$ was used to estimate the crystallite size. Here κ was taken as 0.94, and θhkl as one half of the diffraction angle 2θhkl. Williamson and Smallman's method [16] was used to estimate the dislocation density from the peak profile of each reflection.

2.5.2 Phase fraction

The material has an FCC structure, and no secondary phases or precipitates were detected in the as-built material [13].

2.5.3 Residual stress

There was negligible macroscopic residual stress in a sample of approximate volume $2\,\text{mm} \times 3\,\text{mm} \times 3\,\text{mm}$ [14]. As our meso-tensile specimen were much smaller than this, we felt it was appropriate to assume there was negligible macroscopic residual stress in our meso-tensile specimen.

2.5.4 Single crystal C-tensor

We did not measure single crystal elastic constants for our material. We have found values in the literature, as one option that modelers may choose to use, but that was left to the modelers' discretion. The values found in the literature are for AM IN625 made via directed energy deposition (DED) and are reported as C11 = 243.3 GPa, C12 = 156.7 GPa, and C44 = 117.8 GPa [17]. This source was provided to modellers as an option to use in their model.

2.5.5 Fracture surface analysis

Two analyses of the fracture surface were conducted to measure the width reduction, an indicator of ductility, one of the challenge values requested for models to predict. The fracture width and area were estimated from a XRCT image and from an SEM image. For the XRCT image, a plane near to the fracture surface was selected such that it is was close to the fracture surface as possible without crossing the fracture surface, as schematically shown by the dashed green line in the left pane of Figure 4a). To assess the quality of this selection, a grayscale map of the depth of material from the plane to the fracture surface was construct, as shown in the right pane of Figure 4a). Grayscale value here represents depth of material, with any non-black pixel indicating that there is material. From this, width or area can easily be computed, either by summing the number of non-black pixels along each row to arrive at the width as

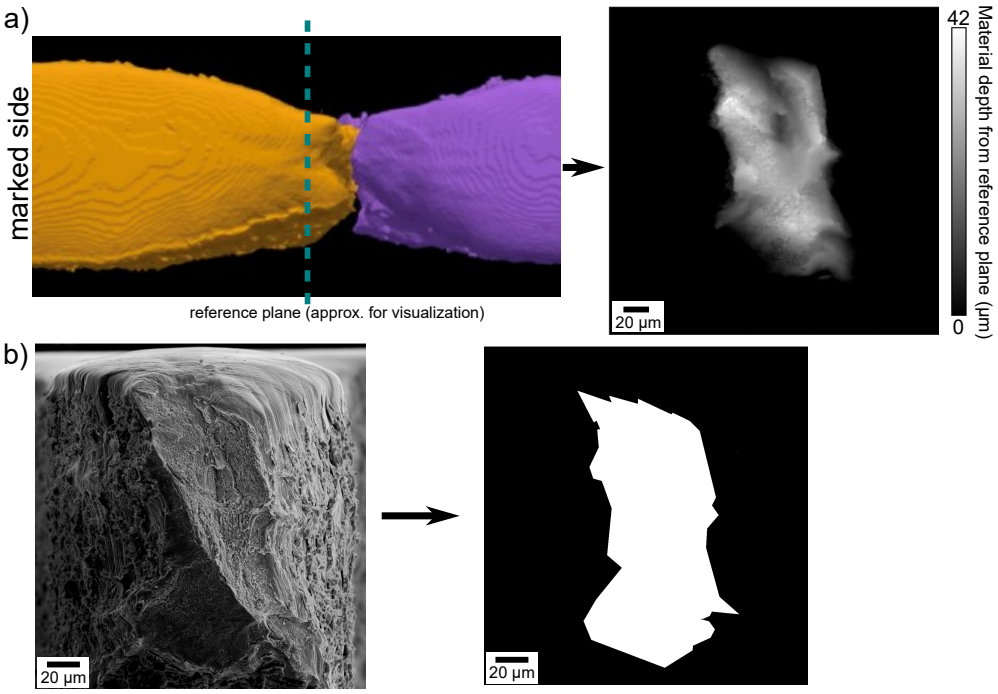

Fig. 4 Measurement of fracture surface with: a) XRCT where the green dashed line approximately represents the reference plane and the grayscale maps indicates the depth of material from that plane to the fracture surface (in this case, the rightward extents of orange material), i.e., anywhere a non-black pixel appears there is material, and the non-black pixels can be used to estimate width or area, to compute width (or area) reduction. b) End-on SEM image of the fracture surface and its estimated outline made by manually drawing a polygon. Again, non-black pixels indicate material and thus can be used to estimate width (or area) reduction.

a function of height, or by counting the total non-black pixels to calculate the area. From the SEM image (Figure 4b, left side), the fracture surface was hand-fit with a polygon to represent the estimated fracture surface as a grayscale (in this case black-and-white) image. This is shown in the right side pane of Figure 4b. An identical procedure as that used to compute width and area from the XRCT grayscale image was used to compute width and area from the polygon derived from the SEM image.

Fracture surface width (i.e., length in the Z-direction) as a function of thickness was thus extracted from both measurements, as shown in Figure 8 in the results section. The mean width between 50 µm and 200 µm through-thickness length for XRCT and between 80 µm and 200 µm for SEM was computed and used to determine the width reduction for the challenge. None of the fracture information collected here was provided to modellers during the competition.

Table 3 Cross-sectional area statistics, in μm^2

Mean	47 611
Minimum	45 320
Standard deviation	3504

3 Experimental Results

Experimental results are segregated into those provided to modellers for the AM Benchmark challenge, and those used for scoring (i.e., held back).

3.1 Results provided to modellers

The build, manufacturing, and chemistry information provided above in Section 2 was provided to modellers, along with the following results.

3.1.1 Metallography

Figure 5a shows an optical image of the pre-test specimen with fiducial marker, as provided to the modellers for orientation specification and context. The stitched EBSD data set from the entire gauge length (XZ plane) is provided in Figure 5b-c. All stitched data sets were provided as .ang files to the modellers, and are accessible via the associated data publication [12]. No cleaning operations were performed on any of the EBSD data. Figure 5d provides an example of the sub-grain structure, visible in the XZ plane. The spacing of the sub-grain structure (columnar dendritic cells formed during rapid solidification) was measured using a line-intercept method where the number of sub-grain structures was counted per 10 µm line segments. Four backscattered electron (BSE) images were captured from random areas along the gauge length and bulk wafer. Thirty lines per BSE iamge were used. The number of sub-grains per micrometer was then converted to a spacing value representing the average spacing between centroids of sub-grain structures. This resulted in an estimated spacing of (0.34 ± 0.09) µm. All images of sub-grain structure and possible re-cast layer are provided in Ref [12].

3.1.2 X-ray CT

Full raw and post-processed (binarized) XRCT images were provided to modellers. A 3D rendering of the image is shown in Figure 3. In addition, summary statistics were provided, i.e., the data shown in Table 3.

3.1.3 Stress-strain information

No specific macroscale stress-strain curves were provided. However, similar material (with a different scan strategy) was tested and calibration stress-strain data provided for the macroscale challenge (see Ref. [18]). Modellers could choose to use the macroscale data from the other challenge, data from literature, or other information at their disposal (short of re-running our tests) as presumed macroscale response information.

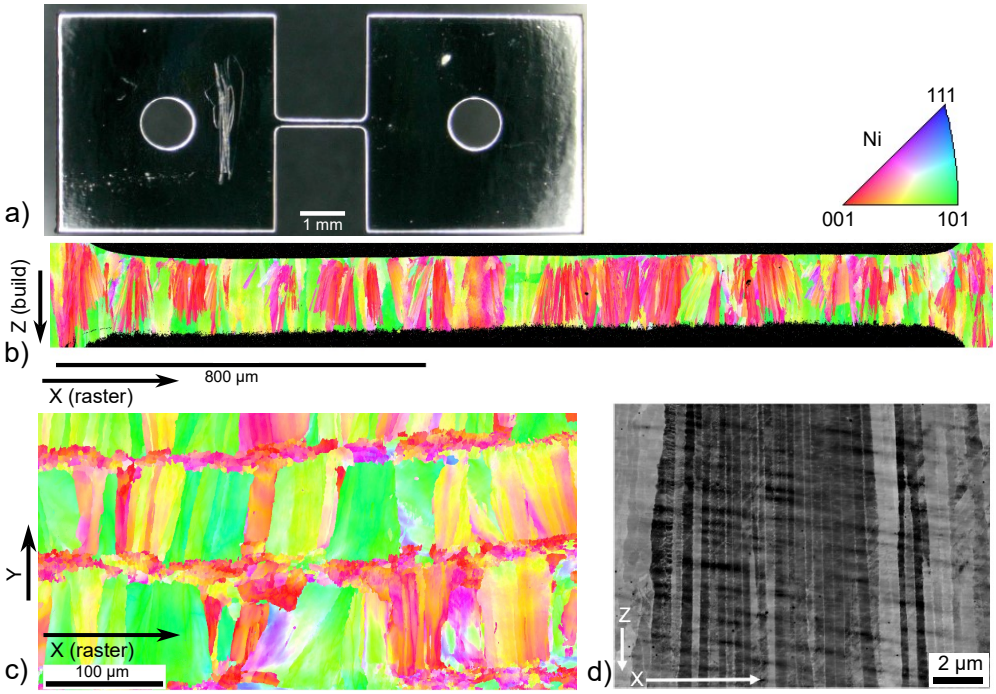

Fig. 5 a) optical image of as-tested specimen (fiducial mark on left side of grip), b) pre-test EBSD of one surface of the specimen, as provided to the challenge participants, c) EBSD of an orthogonal direction (material from the wafer, not the specimen itself), d) representative backscatter electron image of sub-grain microstructure, showing further directionality

3.2 Results Used for Scoring

The following experimental results were held back from the modellers, to enable a fully blind prediction, as described above.

3.2.1 Stress versus strain curve

The overall true stress versus true strain for specimen TH1-F is given in Figure 6, with vertical (stress) and horizontal (strain) error bars representing respective combined standard uncertainty. From this, the specific points requested from the modellers were extracted, as provided in Table 4. The plot only include stress and strain values up to the point of maximum force (although data was captured through failure, its conversion to true values is nonsensical after the onset of necking). Additionally, Young's modulus computed from uniaxial tensile tests is known to be only approximate.

3.2.2 Post-test optical and EBSD images

The failed specimen was imaged again with an optical microscope (Figure 7a) and mapped with EBSD (Figure 7b) to define the failure location. For the challenge, the

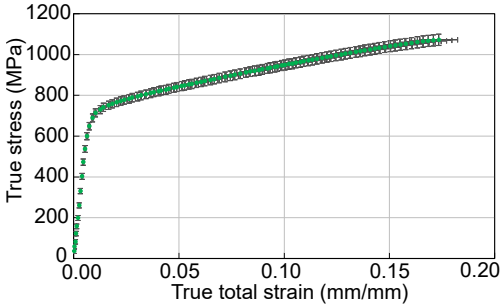

Fig. 6 True stress versus true strain for specimen TH1-F, where stress is computed from the average (mean) area computed from X-ray CT. Error bars represent combined standard uncertainty. Vertical error bars are computed from load cell and area uncertainty, while horizontal error bars are computed from DIC uncertainty. The plot is truncated at the point of maximum force.

Table 4 True stress-true strain properties for TH1-F, computed from mean area and including combined standard uncertainty computed from stress (load cell and area) or strain (DIC) as appropriate.

	from mean area	Combined std uncertainty (%)
Young's modulus (GPa)	102	11
0.002 true strain offset yield strength (MPa)	689	11
True stress at 0.05 true strain (MPa)	841	3
True stress at max force (MPa), data point 92	1073	3
True strain at max force (mm/mm), data point 92	0.1743	6
True stress at onset of necking (MPa), data point 77	1017	3
True strain at onset of necking (mm/mm), data point 77	0.1362	6

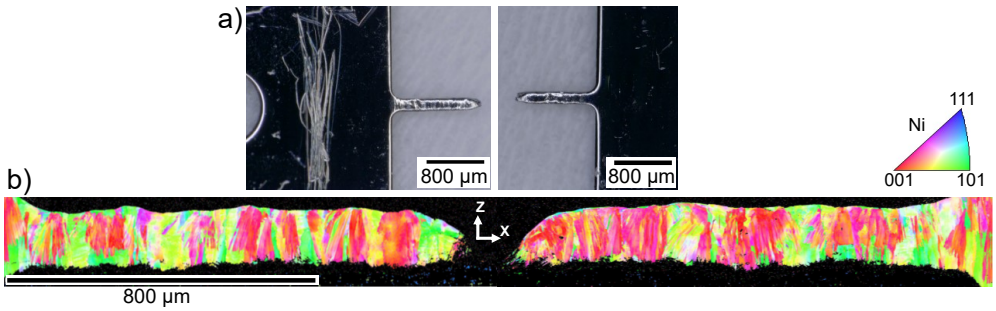

Fig. 7 Post-test images of the failed specimen, with (a) optical microscopy and (b) EBSD grain orientation mapping.

edge of the EBSD map was taken as the 0-point reference, and failure location defined along the +X axis.

3.2.3 Post-test fracture surface analysis

Figure 8 shows the width of the fracture surface as a function of height as measured by the two different techniques. Although the trends are similar, the XRCT gives a

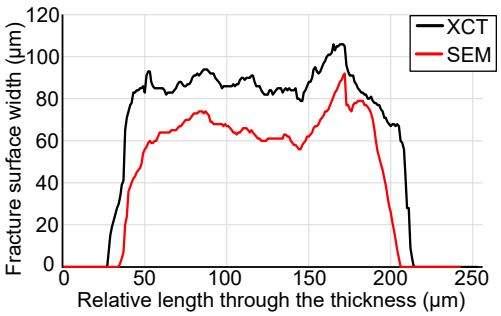

Fig. 8 Fracture surface width through the depth of the specimen. This shows that the SEM and XRCT results are similar, though the SEM is consistently shorter, as expected. From this, mean width reduction was computed.

Table 5 Fracture surface widths as computed from SEM and XRCT for the marked side.

	SEM	XRCT
Max width (µm)	92.0	106
Min width (µm)	56.0	67.0
Mean width (µm)	68.5	87.3
Std Dev width (µm)	7.75	7.28
Width reduction (%)	64.6±4.0	54.9±3.7

slightly larger area—this was expected, because rather than a 2D projection of the surface itself this is a cross-section slightly interior to the failure surface. Table 5 tabulates the fracture surface areas. The SEM-based measurement was used for the challenge, while the secondary XRCT measurement increases confidence in the result.

4 Discussion

4.1 Modeling Submissions

Full descriptions of the models submitted by challenge participants may be described elsewhere in this topical collection. In the following, we will briefly discuss the submissions, but focus on comparisons of the submitted numerical results.

Six submissions were received for the challenge, with five of the six submitting answers for all challenge categories. Each group was randomly assigned a number to uniquely and anonymously identify them in the comparison of results presented below.

The modellers used either finite element analysis or fast Fourier transform based techniques to solve the mechanics equations. Crystal plasticity was chosen as the material law in all cases, with minor permutations: although most groups used power-law hardening, dislocation density based hardening was also used. Some teams used different techniques for different parts of the challenge, for instance using a damage model to predict failure separately from the crystal plasticity simulation for mechanical properties. Only one team provided for uncertainty in their approach.

Assumptions used by the modellers was one of the main differentiating factors, although the results suggest that no one approach was overall more successful than

any other. Most teams employed some form of mesh study to determine sensitivity to element size, and all teams down-sampled the EBSD data to achieve tractable grain counts. Most groups used voxel meshes, which may result in unwanted grain boundary interface effects (these details were not reported, however). Although all teams made use of the EBSD data provided, some used the statistics to produce multiple representative instantiations of possible 3D microstructures, while others directly used the 2D data provided or extrapolated the 2D representation into 3D. Direct use of the XRCT data was uncommon, although it was used to define the exact shape of the specimen by at least one of the modelling teams. All groups used roughly the same boundary conditions: one side of the gauge section held fixed, and displacement applied to the other side. The grip sections of the specimen were not included in any model, leaving the potential influence of the pin-loaded condition unexplored.

4.2 Analysis of Model Submission Results

The overall results for models predicting the stress-strain curve summary statistics (up until ultimate strength, see Section 1 for summary points requested) are shown in Figure 9a-e. More highly correlated factors, such as stress at 0.05 strain and yield stress, had consistent trends between groups. However, no one group was closest to the measurement value(s) for all cases. Most measures, with the exception of elastic modulus, had a range of responses both over- and under-predicting the measured values. Elastic modulus was consistently over-predicted. Although the exact reason for this is not clear, we suspect it may be related to the anisotropy in the grain structure and the fact that only 2D grain information was provided. It may also be related to the elastic behavior available to the modellers for calibration - the models using literature data (not the macroscale data provided in CHAL-AMB2022-04-MaTTO [18]) for calibration seem to have performed somewhat better. All models achieve a relatively close prediction of yield stress, considering the limited calibration data provided. This is likely because crystal plasticity models specifically and directly calibrate this value: they usually contain a term that governs slip initiation. Nevertheless, this is promising in terms of the applicability of CP models to prediction of macroscale phenomena of practical interest, such as onset of localized plasticity, at least under simple loading conditions.

Figure 9f summarizes the width reduction at failure results, while Figure 10 shows the fracture location predictions and compares them to the measured failure and necking start/end locations. Both factors proved substantially more difficult to model than the elastoplastic regime response. This is perhaps related to multiple factors. Localization and fracture in these sub-scale specimens is highly dependant on local microstructure, and although 3D XRCT was provided, only 2D grains were measured and provided. This limits the models' ability to accurately compute stress concentrations from grain boundary interfaces. Although a surface grain boundary appears to have been the failure location, the specific grain boundary responsible for failure likely depends on sub-surface structures, which were not measured in this work. Width reduction may be somewhat less microstructurally determined, but poses a significant challenge on the models—the reduction in area is related to strain to failure, and without a damage model or means to separate elements, computational model predictions

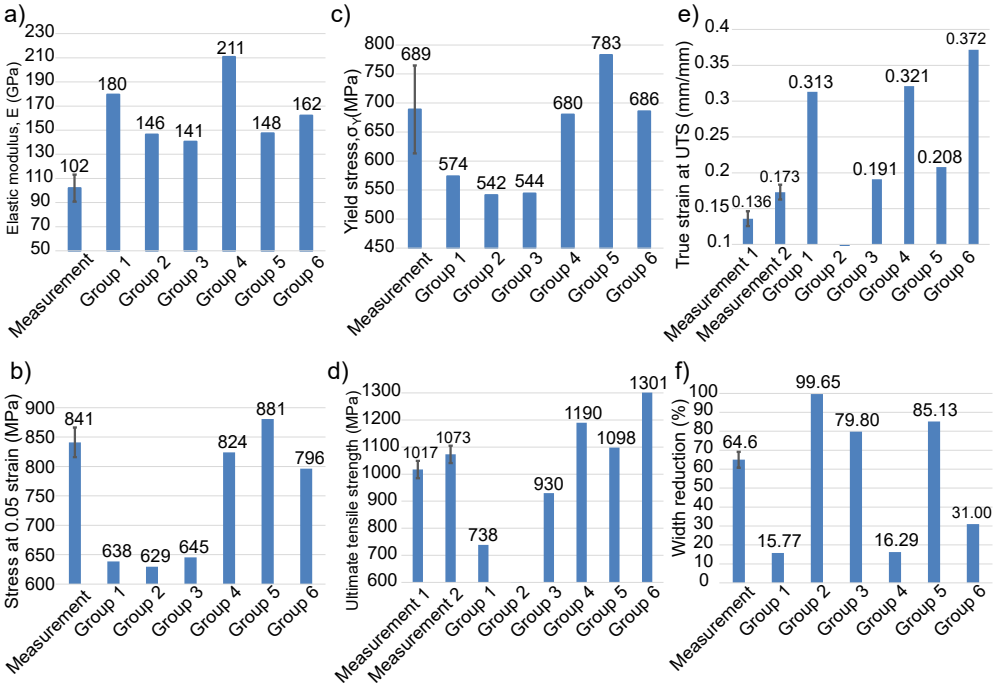

Fig. 9 Comparison of predicted values to measurements. a) Elastic modulus, b) true stress at 0.05 true strain, c) yield stress, d) ultimate tensile strength (true stress value), e) true strain at UTS, f) width reduction from fracture analysis (error bar represents standard deviation of fracture surface width through the thickness). d) and e) have two measurements: measurement 1 corresponds to the onset of necking; measurement 2 corresponds to maximum force. Error bars on the measurements represent combined standard uncertainty unless noted otherwise.

will depend highly on the modellers' choice of when to stop the computation rather than any physical mechanism. Most modellers chose to use plastic strain as a proxy for the damage zone, with mixed efficacy. This appeared to be a major determining factor for the width reduction part of the challenge, where strain to failure was not provided. Prediction of ductility is, perhaps, one of the more challenging elements of computational crystal plasticity, and the large spread in challenge results represents this.

4.3 Lesson Learned and Future Directions

Through discussions with modeller participants during Q&A sessions, the AM Bench 2022 conference, and a post-challenge workshop we hosted to recap, several areas for improvement have been identified. These are procedural as well as to do with challenge information.

- More points of communication with participants. It would be helpful to have more open forums for communication between challenge participants and the challenge

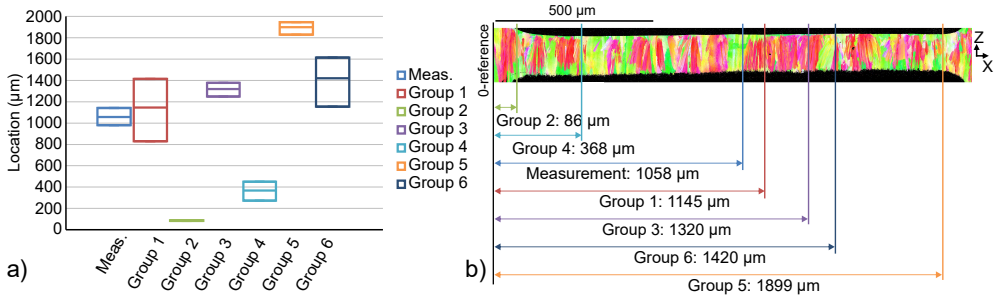

Fig. 10 Fracture location measurement and predictions: a) color-coded by group, this chart shows the fracture location prediction as the mid-bar and the extents of the necking region as the top and bottom bars for the measurement and each prediction; b) visualizes these predictions with respect to the undeformed EBSD map, showing the specific grains at which the measurement and each model observed/predicted fracture.

team, mostly for clarifying or providing added information if something was omitted from the initial descriptions. Care must be taken to avoid providing unequal information to participants. Ideas such as multiple Q&A sessions throughout the submission window, or a public, website-based system where participants can ask questions will be considered.

- Continue optimizing information delivery in the initial challenge statement. Although the challenge statement was fairly encompassing, a few details such as registration of the XRCT data and EBSD data could have been improved.
- Some suggested that the calibration information was lacking. There is a difficult line to be drawn between enough calibration information and maintaining truly blind *predictions*. We will continue to assess the balance of provided and withheld information in future challenges.
- One major, though practically realistic, limitation was that only 2D grain information was provided, albeit for two orthogonal planes. The results, and modeller themselves, suggest this substantially hinders predictive abilities. It does, however, provide some insight into the capabilities of microstructure-based paradigms given scarce data, which is a practically relevant concern. That said, one avenue of future work will be to work towards providing 3D grain information at a resolution that quantifies intragranular misorientation.

5 Conclusion

The goal of this manuscript has been to describe the subcontinuum tensile additive manufacturing benchmark challenge of 2022, from the perspective of the challenge organizers, and to provide insight into the results of the challenge itself. The experimental descriptions themselves closely mirror those of the dataset published in support of the challenge, describing specimen production, measurements, testing, and results. The second part of the paper outlines the challenge participants' contributions, and compares them to the measured results for the blind part of the dataset.

We have found that blind predictions of subcontinuum mechanical properties are possible, though challenging. Care must be taken in defining the physical laws governing the behavior and the data used to parametrically fit these laws to a material of interest. Moreover, it is possible, or even likely, that models with an accurate prediction of one part of the stress-strain curve are inaccurate elsewhere. Although there were limitations on the data provided, these limitations represent practically realistic data upon which models might be expected to base predictions. The results here can be interpreted as promising: showing the potential for microstructural models to predict mechanical performance. The results should also be seen as motivational, in that wider adoption of such techniques will depend on improving their ability to ingest practically collectable information and using that to model mechanical behavior with more accuracy. In particular, the broad spread of prediction results for the fracture location may be based on insufficient information, but certainly points to a current fundamental limitation of these models. Possible enhancements may involve direct incorporation of physical damage and failure mechanisms, or more empirically based means to reasonably bound material behavior at the failure limit. Finally, one major area for improvement would be estimates of uncertainty of the model prediction. This was not requested in the current challenge, and we did not expect it, but being able to assess the quality of the model on the basis of the information provided (or lack thereof) during model construction would provide very meaningful insight into the capabilities of a given prediction.

Supplementary information. All additional information has been published in the associated data set [12].

Acknowledgments. We thank Lyle Levine for coordinating and running the overall AM Benchmark series, of which this was part.

Declarations

Funding:

NIST provided all funding needed for this research.

Conflict of interest:

On behalf of all authors, the corresponding author states that there is no conflict of interest.

Ethics approval:

This work has been reviewed by the NIST Editorial Review Board and found acceptably for publication.

Consent for publication:

All authors have read and agree to the contents of this manuscript.

Availability of data and materials:

All data are published at [12]. Materials are all available to the public and have been as thoroughly identified as possible to facilitate reproduction of the work.

Code availability:

Code and some raw data has been shared in [11] and [12]. Commercial codes (e.g., EBSD analysis) have been identified where possible. Code and some raw data for DIC data processing (strain measurement) has been withheld for legal reasons (see [9]), although devising a way to publish these codes is under way.

Authors' contributions:

OLK: conceptualization and design, XRCT, analysis, writing/editing; JTB: conceptualization and design, sample preparation, SEM, EBSD, writing/editing; NM: conceptualization and design, XRCT; LAL: sample design, mechanical testing and data analysis; JW: conceptualization, part fabrication; NH: conceptualization and design, project management and organization.

References

[1] Gesing, M., Gilkey, L.N., Jones, C.A., Dingreville, R., Sanborn, S.E., Bignell, J.L., Cerrone, A.R., Keim, V., Nonn, A., Cooreman, S., Thibaux, P., Ames, N., Connor, D.O., Parno, M., Davis, B., Tucker, J., Coudrillier, B., Karlson, K.N., Ostien, J.T., Foulk, J.W., Hammetter, C.I., Grange, S., Emery, J.M., Brown, J.A., Bishop, J.E., Johnson, K.L., Ford, K.R., Brinckmann, S., Neilsen, M.K., Jackiewicz, J., Ravi-Chandar, K., Ivanoff, T., Salzbrenner, B.C., Boyce, B.: The third sandia fracture challenge: predictions of ductile fracture in additively manufactured metal. International Journal of Fracture **218** (2019) https://doi.org/10.1007/s10704-019-00361-1

[2] Cox, M.E., Schwalbach, E.J., Blaiszik, B.J., Groeber, M.A.: AFRL Additive Manufacturing Modeling Challenge Series: Overview. Integrating Materials and Manufacturing Innovation **10** (2021) https://doi.org/10.1007/s40192-021-00215-6

[3] Levine, L., Lane, B., Heigel, J., Migler, K., Stoudt, M., Phan, T., Ricker, R., Strantza, M., Hill, M., Zhang, F., Seppala, J., Garboczi, E., Bain, E., Cole, D., Allen, A., Fox, J., Campbell, C.: Outcomes and Conclusions from the 2018 AM-Bench Measurements, Challenge Problems, Modeling Submissions, and Conference. Integrating Materials and Manufacturing Innovation **9**(1), 1–15 (2020) https://doi.org/10.1007/s40192-019-00164-1

[4] Committee, A.E.: ASTM E1479-16: Standard Practice for Describing and Specifying Inductively Coupled Plasma Atomic Emission Spectrometers (2016) https://doi.org/10.1520/E1479-16

[5] Committee, A.E.: ASTM E1019-18: Standard Test Methods for Determination of Carbon, Sulfur, Nitrogen, and Oxygen in Steel, Iron, Nickel, and Cobalt Alloys

by Various Combustion and Inert Gas Fusion Techniques (2018) https://doi.org/10.1520/E1019-18

[6] Committee, A.B.: ASTM B564-22: Standard Specification for Nickel Alloy Forgings (2022) https://doi.org/10.1520/B0564-22

[7] Liew, L.-A., Read, D.T., Martin, M.L., DelRio, F.W., Bradley, P.E., Barbosa, N., Christenson, T.R., Geaney, J.T.: Elastic-plastic properties of mesoscale electrodeposited LIGA nickel alloy films: microscopy and mechanics. J. Micromech. Microeng. **31**(1), 015002 (2020) https://doi.org/10.1088/1361-6439/abc0ff . Publisher: IOP Publishing

[8] Benzing, J.T., Liew, L.A., Hrabe, N., DelRio, F.W.: Tracking Defects and Microstructural Heterogeneities in Meso-Scale Tensile Specimens Excised from Additively Manufactured Parts. Exp Mech **60**(2), 165–170 (2020) https://doi.org/10.1007/s11340-019-00558-4

[9] Liew, L.-A., Read, D.T., Martin, M.L., Christenson, T.R., Geaney, J.T.: Microfabricated fiducial markers for digital image correlation-based micromechanical testing of LIGA Ni alloys. Eng. Res. Express **3**(2), 025019 (2021) https://doi.org/10.1088/2631-8695/abfb10 . Publisher: IOP Publishing

[10] Liew, L.-A., Read, D.T., Martin, M.L., Bradley, P.E., Geaney, J.T.: Elastic–Plastic Properties of Mesoscale Electrodeposited LIGA Nickel Alloy Films: Analysis of Measurement Uncertainties. Journal of Verification, Validation and Uncertainty Quantification **8**(1), 011005 (2023) https://doi.org/10.1115/1.4062106

[11] Moser, N.H., Landauer, A.K., Kafka, O.L.: Image processing in Python for 3D image stacks (Imppy3d). National Institute of Standards and Technology (2023). https://doi.org/10.18434/mds2-2806 . https://github.com/usnistgov/imppy3d

[12] AM Bench 2022 challenge problem Subcontinuum Mesoscale Tensile Test (CHALAMB2022-04-MeTT). National Institute of Standards and Technology https://doi.org/10.18434/mds2-2587

[13] Zhang, F., Levine, L.E., Allen, A.J., Young, S.W., Williams, M.E., Stoudt, M.R., Moon, K.-W., Heigel, J.C., Ilavsky, J.: Phase Fraction and Evolution of Additively Manufactured (AM) 15-5 Stainless Steel and Inconel 625 AM-Bench Artifacts. Integr Mater Manuf Innov **8**(3), 362–377 (2019) https://doi.org/10.1007/s40192-019-00148-1

[14] Phan, T.Q., Strantza, M., Hill, M.R., Gnaupel-Herold, T.H., Heigel, J., D'Elia, C.R., DeWald, A.T., Clausen, B., Pagan, D.C., Peter Ko, J.Y., Brown, D.W., Levine, L.E.: Elastic Residual Strain and Stress Measurements and Corresponding Part Deflections of 3D Additive Manufacturing Builds of IN625 AM-Bench

Artifacts Using Neutron Diffraction, Synchrotron X-Ray Diffraction, and Contour Method. Integr Mater Manuf Innov **8**(3), 318–334 (2019) https://doi.org/10.1007/s40192-019-00149-0

[15] Lee, P.L., Shu, D., Ramanathan, M., Preissner, C., Wang, J., Beno, M.A., Von Dreele, R.B., Ribaud, L., Kurtz, C., Antao, S.M., Jiao, X., Toby, B.H.: A twelve-analyzer detector system for high-resolution powder diffraction. J Synchrotron Rad **15**(5), 427–432 (2008) https://doi.org/10.1107/S0909049508018438

[16] Williamson, G.K., Smallman, R.E.: III. Dislocation densities in some annealed and cold-worked metals from measurements on the X-ray debye-scherrer spectrum. The Philosophical Magazine: A Journal of Theoretical Experimental and Applied Physics **1**(1), 34–46 (1956) https://doi.org/10.1080/14786435608238074 . Publisher: Taylor & Francis _eprint: https://doi.org/10.1080/14786435608238074

[17] Wang, Z., Stoica, A.D., Ma, D., Beese, A.M.: Diffraction and single-crystal elastic constants of Inconel 625 at room and elevated temperatures determined by neutron diffraction. Materials Science and Engineering: A **674**, 406–412 (2016) https://doi.org/10.1016/j.msea.2016.08.010

[18] AM Bench 2022 challenge Macroscale Tensile Tests at Different Orientations (CHAL-AMB2022-04-MaTTO). National Institute of Standards and Technology https://doi.org/10.18434/mds2-2588

A DIC parameters

Table 6 reports the relevant DIC parameters used for 2-point extensometry style strain measurement.

Table 6 DIC parameters for strain measurements. [1]Criterion of 10% of a speckle size on the image, which for this AM specimen was about 12 pixels for the smaller features. [2]From stationary images, and from the displacement during exposure.

Camera	Jenoptik ProgRes C7 camera (S/N 2708-47-0124)
Objective	Mitutoyo 2X M Plan Apochromatic objective, N.A. 0.055, W.D. 34 mm
FOV (measured in test setup)	4.4 mm
Calibration (with ruled glass from LECO)	693 pixels/mm
DIC subset size	64 pixels × 64 pixels
Step size	0 (only one subset)
Subset shape function	likely bilinear or bicubic (details uncertain)
Acceptable noise floor[1]	1.2 pixels
Actual noise floor[2]	0.05 pixels to 0.1 pixels
Image filtering	none